

# Geologic controls of slow-moving landslides near the US West Coast



**Abstract** Slow-moving landslides, often with nearly imperceptible creeping motion, are an important landscape shaper and a dangerous natural hazard across the globe, yet their spatial distribution and geologic controls are still poorly known owing to a paucity of detailed, large-area observations. Here, we use interferometry of L-band satellite radar images to reveal 617 spatially large ( $4 \times 10^4$ – $13 \times 10^6$  m<sup>2</sup>) and presently active (2007–2019) slow-moving landslides near the populous US West Coast (only 4.6% of these slides were previously known) and provide evidence for their fundamental controls by bedrock lithology and vertical land motion. We found that slow-moving landslides are generally larger and more spatially frequent in homogeneous bedrock with low rock strength, and they are preferentially located on hillslopes with geologically recent uplift. Notably, landslide size and spatial density in the relatively weak metamorphic rocks and *mélange* (due to pervasive tectonically sheared discontinuities, foliation, and abundant clay minerals) were two times larger than those in sedimentary and igneous rocks, and the hillslopes with landslides were found to be uplifting approximately three times faster than the average for the whole region. These results suggest that slow-moving landslides can be effectively uncovered by satellite radar imagery and their occurrence and character may be anticipated from vertical land uplift and bedrock lithology. Hence, our study provides understanding critical for reducing landslide hazards and quantifying landslide impacts on landscape change.

**Keywords** Bedrock lithology · Land uplift · Radar interferometry · Geomorphic change · Natural hazards

## Introduction

Landslides are a geologic process crucial for landscape evolution (Burbank et al. 1996; Kelsey and Bockheim 1994; Roering et al. 2009; Simoni et al. 2013), and as a natural hazard, landslides annually cause 3.5 billion dollars of property loss and 25–50 casualties in the USA alone (Spiker and Gori 2003). Locating presently active landslides is a critical step towards preventing their future hazards and forecasting their impact on the landscape. However, conventional landslide-identifying approaches that rely on geologic maps and citizen-reported events (Guzzetti et al. 2012; Highland and Bobrowsky 2008; Jones et al. 2019) could easily miss numerous active yet slowly moving slides that lack readily identifiable features (e.g., fresh headscarps) or occur in rarely accessed lands. Slow-moving landslides persistently damage infrastructure and imply a force imbalance of the hillslope (Highland and Bobrowsky 2008). Additional forces such as earthquake shaking, coastal and stream erosion, intense rainfall, and other natural or anthropogenic disturbance could shift their present creeping behavior into rapid movement and cause catastrophic damages (e.g., Intrieri et al. 2018; Kilburn and Petley 2003; Schulz and Wang 2014; Xu et al. 2020b). Discovering presently slow-moving landslides for future hazard prevention particularly requires approaches with high

measurement accuracy and wide spatial coverage. However, few tools were available until the InSAR (Interferometric Synthetic Aperture Radar) method evolved into an effective means in the last two decades (Handwerger et al. 2019; Intrieri et al. 2018; Squarzoni et al. 2003; Xu et al. 2019, 2020b; Ye et al. 2004). InSAR utilizes interferometry of satellite-captured radar images (frequent repeated acquisitions since 1992) to achieve maximal millimeter-level measurements of ground displacement along the radar line-of-sight (LOS) direction (Ferretti et al. 2007; Nishiguchi et al. 2017).

Multiple studies have focused on the precipitation-driven short-timescale dynamics of presently active, slow-moving landslides (e.g., Bennett et al. 2016b; Handwerger et al. 2019; Kang et al. 2021; Mackey et al. 2009; Squarzoni et al. 2003; Xu et al. 2020b; Ye et al. 2004); however, knowledge of their geologic controls is still poorly known owing to a lack of detailed, large-scale evidence, but such knowledge is essential for deciphering their characteristics and for preventing future hazards. Spatially large, slow-moving landslides are generally deep-seated (meters to hundreds of meters) (Bonzanigo et al. 2007; Highland and Bobrowsky 2008; Larsen et al. 2010) and may have been active for hundreds to thousands of years (Bonzanigo et al. 2007; Bovis and Jones 1992; Kelsey and Bockheim 1994; Mackey et al. 2009; Varnes and Savage 1996). Hence, their occurrence could be controlled by the lithology and structure of the underlying bedrock and by geologic processes (Clarke and Burbank 2010; Cruden and Varnes 1996; Lambe and Whitman 1969; Roering et al. 2005). In addition, vertical uplift (i.e., any upward movement of the land surface) in a geologic timescale ( $10^3$ – $10^5$  years) could deliberately alter the force balance of hillslopes and regulate the denudation process (Burbank et al. 1996; Bennett et al. 2016a; Larsen and Montgomery 2012; Roering et al. 2015), thereby potentially modulating occurrence and kinematics of long-term creeping landslides.

Here, we apply the high-accuracy InSAR method over the entire US West Coast states ( $\sim 8.6 \times 10^5$  km<sup>2</sup>) to discover large, presently active landslides in both the high mountains and coastal neighborhoods inhabited by 47.8 million people (2019 census; USCB 2019). Based on the large-scale observations, we tested our hypotheses that the spatial density and size of slow-moving landslides are significantly controlled by bedrock type and that their occurrence and persistent motion reflect long-term land uplift.

## Materials and methods

### SAR interferogram generation and unwrapping

We used radar interferometry of both the ALOS PALSAR (Advanced Land Observing Satellite-Phased Array type L-band Synthetic Aperture Radar) images from 2007 to 2011 and ALOS-2 PALSAR-2 images from 2015 to 2019 for identifying landslides near the US West Coast. The L-band SAR images were primarily utilized over the relatively densely vegetated US West Coast because of L-band

sensor's capability in vegetation penetration. SAR interferograms were generated by differencing the phase measurements of two SAR images. For each SAR interferogram, the interferometric phase of a SAR resolution element,  $\phi$ , is composed of multiple independent components:

$$\phi = W\{\phi_{\text{def}} + \phi_{\text{dem}} + \phi_{\text{orb}} + \phi_{\text{atm}} + \phi_{\text{n}}\} \quad (1)$$

where  $\phi_{\text{def}}$  is the phase change due to movement of the pixel in the satellite radar line-of-sight direction;  $\phi_{\text{dem}}$  is the DEM (digital elevation model) error sourcing from the difference between the DEM height and the elevation of average scatterers in the resolution element;  $\phi_{\text{orb}}$  is the residual phase due to orbit errors;  $\phi_{\text{atm}}$  is the difference in atmospheric phase delay between passes;  $\phi_{\text{n}}$  is the phase noise due to both temporal variability in scattering and thermal noise; and  $W\{\cdot\}$  is the wrapping operator that drops whole phase cycles ( $2\pi$ ), as only a fractional part of a cycle can be measured with SAR interferometry. In order to obtain  $\phi_{\text{def}}$ , other contributing terms including  $\phi_{\text{dem}}$ ,  $\phi_{\text{orb}}$ ,  $\phi_{\text{atm}}$ , and  $\phi_{\text{n}}$  must be removed or reduced.

We set multi-looking factors of  $3 \times 7$  (range by azimuth) and  $2 \times 4$  for ALOS PALSAR and ALOS-2 PALSAR-2 images, respectively, in order to reduce the approximately Gaussian-distributed data noise  $\phi_{\text{n}}$  (Hanssen 2001). We also minimized the DEM contributions  $\phi_{\text{dem}}$  by using the 1-arcsec SRTM DEMs (Farr et al. 2007) and reduced the orbit-related artifacts  $\phi_{\text{orb}}$  using the quadratic fitting (Fattahi and Amelung 2014). The stratified atmospheric artifacts related to regional topography were reduced by using a linear fitting, and other large-spatial-scale phase artifacts such as tropospheric noises were largely reduced by selecting localized, stable, and highly coherent reference regions near the landslides. We unwrapped the SAR interferograms through the minimum cost flow approach (Costantini 1998) using the GAMMA software (Werner et al. 2000) and set a coherence threshold of 0.4 for both ALOS and ALOS-2 interferograms. Accuracy of the InSAR measurement can be quantified based on the Cramer-Rao bound (Rodriguez and Martin 1992):

$$\sigma = \frac{\lambda}{4\pi} \sqrt{\frac{1}{2NM} \frac{(1-\gamma^2)}{\gamma^2}} \quad (2)$$

where  $\sigma$  is the uncertainty of InSAR measurements,  $\lambda$  the radar wavelength,  $N$  and  $M$  the window sizes for the coherence estimation, and  $\gamma$  the coherence. We used a  $32 \times 32$  moving window for the coherence estimation, which consequently corresponds to a minimum measurement uncertainty of  $\sim 1.4$  mm for both ALOS and ALOS-2 data.

### Identification of active landslides

Active landslides were identified based on the ground motion captured by SAR interferograms. All of the interferograms with good coherence (greater than 0.4) and with various temporal (maximum timespan of 2 years) and perpendicular baselines were utilized to cross-validate the identified landslides. We also used the 10-m-resolution DEMs (USGS 2020b) from the US Geological Survey and the high-resolution true color image time series from Google Earth to exclude non-landsliding displacement signals dominated by processes such as vegetation regrowth after clear cut, water level change in wetlands, underground mining and oil exploitation, and urban construction. Note that rapid landslides such as rock

avalanches and debris flows that alter original ground features significantly leading to complete coherence loss are not identifiable from SAR interferograms. The active landslide boundaries were firstly outlined through thresholding radar LOS deformation (greater than 5 mm), and then manually revised by integrating information from Google Earth optical images and the 10-m-resolution DEMs.

### Bedrock of the landslides

Bedrock formations of the identified landslides were derived from the 1:50,000 to 1:1,000,000 scale State Geologic Map Compilation (SGMC) geodatabase of the conterminous United States (ver. 1.1, August 2017) (Horton et al. 2017). We combined the results for essentially repeated geologic formations (e.g., multiple "basalts") and used adjacent hillslope material to revise the formation for eleven landslides that were supposedly in alluvium but actually appeared to have been deposited on alluvium (Supplementary Material Table S1).

### Landslide area-volume scaling and average slope angle

A power-law relationship between landslide volume,  $V$ , and landslide surface area,  $A$ , was used to estimate landslide volumes in varied bedrock (Larsen et al. 2010):

$$V \propto A^\gamma \quad (3)$$

where  $\gamma$  is a scaling exponent. We used  $\gamma = 1.6$  for the identified large, deep-seated landslides (Larsen et al. 2010). Surface areas of landslides were computed from the landslide boundary (see data release in Xu et al. 2020b) outlined from SAR interferograms.

The slope angle of each DEM cell element was derived from the 10-m-resolution DEMs. Each identified landslide spatially covers multiple DEM cell elements, and we define the average slope angle of a landslide as the arithmetic mean of all cell elements within the landslide boundary.

### Land uplift rate

Land uplift rates over the US West Coast were obtained by evaluating published literature on geologically and historically recent vertical land movement. This literature (Table 1) includes studies emphasizing land surface surveying (Amos et al. 2014; Hammond et al. 2016; Levy 2019; Yousefi et al. 2020) during recent times, or geologic studies generally extending from recent times into the Quaternary and Neogene Periods (Amos et al. 2014; Anderson 2008; Barth and May 1992; Bennett et al. 2016a; Hellwig 2010; House 1999; Jones 1987; Kelsey and Bockheim 1994; Kobor and Roering 2004; Levy 2019; Lock et al. 2006; Machette et al. 2008; Muhs et al. 1992; Pazzaglia and Brandon 2001; Penserini et al. 2017; Reiners et al. 2002; Schweickert 2009; Spotila et al. 1998; Unruh 1991; Yousefi et al. 2020). Longer-term studies emphasized fluvial and coastal geomorphology, often with cosmogenic nuclide and/or radionuclide dating, thermochronology, and modeling. We interpolated these pointwise uplift data into a gridded raster file using inverse distance weighting, and we clipped the gridded data to within 100 km of the points, to land sloped more steeply than  $5^\circ$ , and by the geographical boundary of the US West Coast states.

**Table 1** Source literature of the uplift data for the US West Coast

Literature	Primary time period
Amos et al. 2014	Recent
Anderson 2008	Neogene–recent
Barth and May 1992	Cretaceous
Bennett et al. 2016a	Neogene–recent
Hammond et al. 2016	Recent
Hellwig 2010	Pleistocene–recent
House 1999	Cenozoic
Jones 1987	Neogene–recent
Kelsey and Bockheim 1994	Quaternary
Kobor and Roering 2004	Quaternary
Levy 2019	Recent
Lock et al. 2006	Neogene–Quaternary
Machette et al. 2008	Quaternary
Muhs et al. 1992	Quaternary
Pazzaglia and Brandon 2001	Quaternary
Penserini et al. 2017	Recent
Reiners et al. 2002	Tertiary–recent
Roering et al. 2015	Recent
Schweickert 2009	Pliocene–recent
Spotila et al. 1998	Neogene–recent
Unruh 1991	Neogene–recent
Yousefi et al. 2020	Holocene

## Results

### Discovery of actively slow-moving landslides

We processed 6589 scenes of ascending ALOS PALSAR images acquired between 2007 and 2011, and 484 scenes of ALOS-2 PALSAR-2 images acquired between 2015 and 2019 using the InSAR method to discover large, active landslides over the entire US West Coast states (Fig. 1a). Active landslides during the observation period were identified from deformation signals captured by the differential InSAR interferograms, assisted by 10-m-resolution DEMs (digital elevation models) (USGS 2020b) and high-resolution optical satellite images.

We identified 617 landslides in total, of which 375 were active between 2007 and 2011, 471 were active between 2015 and 2019, and 229 were active during both the 2007–2011 and 2015–2019 periods (the exact active areas might slightly vary) (Figs. 1 and 2). Spatially, the landslides are spread out over the US West Coast states, with concentrations in mountain ranges of western Washington, southwestern Oregon, and northwestern California (Fig. 2b). Multiple towns and

roads in especially northern Washington, northwestern California, and the vicinity of the coastline are within 0.5–5 km to the identified landslides (Figs. 1 and 2), and could be threatened by future failure events that initiate rapid slides and flows to travel kilometers (Legros 2002) downslope/downstream. Moreover, comparison with Google Earth optical images reveals numerous infrastructures which are located on the identified active landslides. In addition to the 617 landslides, we also identified 89 active rock glaciers that are predominantly distributed along the high mountain ridges in eastern California (Fig. 2). Overall, these InSAR-captured active landslides are spatially large and some are on relatively steep slopes, which imply high hazard potentials to the vicinity during possible future runoff events. Spatial sizes of the identified landslides range from  $4 \times 10^4$  m<sup>2</sup> to  $13 \times 10^6$  m<sup>2</sup>, and 88.7% are larger than 10<sup>5</sup> m<sup>2</sup>. The majority of the landslides (97.1%) have slope angles between 5 and 30°, and 16.8% (106 slides) are steeper than 20° (Fig. 3).

Of the 617 detected landslides, only 29 (comprising 4.7%) are included in the national landslide geodatabase (Jones et al. 2019), which is a compilation of currently existing, non-systematically mapped global, national, and regional-level landslide inventories (Fig. 1b). The 89 active rock glaciers were also absent. A key reason that most of our identified landslides are missing from the geodatabase is that many of these landslide inventories source from human-reported events and geologic maps (Jones et al. 2019), yet only landslides with historical failures or obvious geomorphic signatures would typically have been noticed and reported. Consequently, long-term, slow or creeping landslide movement are less readily recognized (Highland and Bobrowsky 2008; Keefer and Johnson 1983) so are relatively infrequently discovered. Indeed, our results show that many landslides that we discovered are nearly indistinguishable from their neighboring stable hillslopes on the high-resolution optical images, but their active slow motions (4–17 cm/year along radar line-of-sight direction) were clearly captured and measured by the InSAR interferograms (e.g., Fig. 4). Downslope movement rates of the identified landslides range from millimeters to several meters per year depending on the exact location within a landslide, which correspond to the categories spanning from extremely slow to slow landslides (less than  $5 \times 10^{-3}$  m/s) as defined in Cruden and Varnes 1996. Note that the free and frequently acquired SAR datasets (3–60 repeated acquisitions per year since 1992) also allow identifying the presently active section of a landslide, which is less achievable from LiDAR hillshade maps. In addition, many landslides recorded in the existing geodatabase (Jones et al. 2019) since 1932 were one-time failures such as flows and avalanches that will probably not recur (Cruden and Varnes 1996), while the InSAR-captured large, slow-moving slides are likely to remain active in the near future (Bovis and Jones 1992; Kelsey and Bockheim 1994; Mackey et al. 2009; Varnes and Savage 1996) and pose continued threats.

### Bedrock control of slow-moving landslides

Using the SGMC (State Geologic Map Compilation) geodatabase of the conterminous United States (Horton et al. 2017), we statistically analyzed the bedrock underlying the identified slow-moving landslides. Over the entire study area, 102 out of the total 398 bedrock formations contain landslides, and 16 formations contain more than 10 landslides. Statistically, these 16 formations harbor 484 of

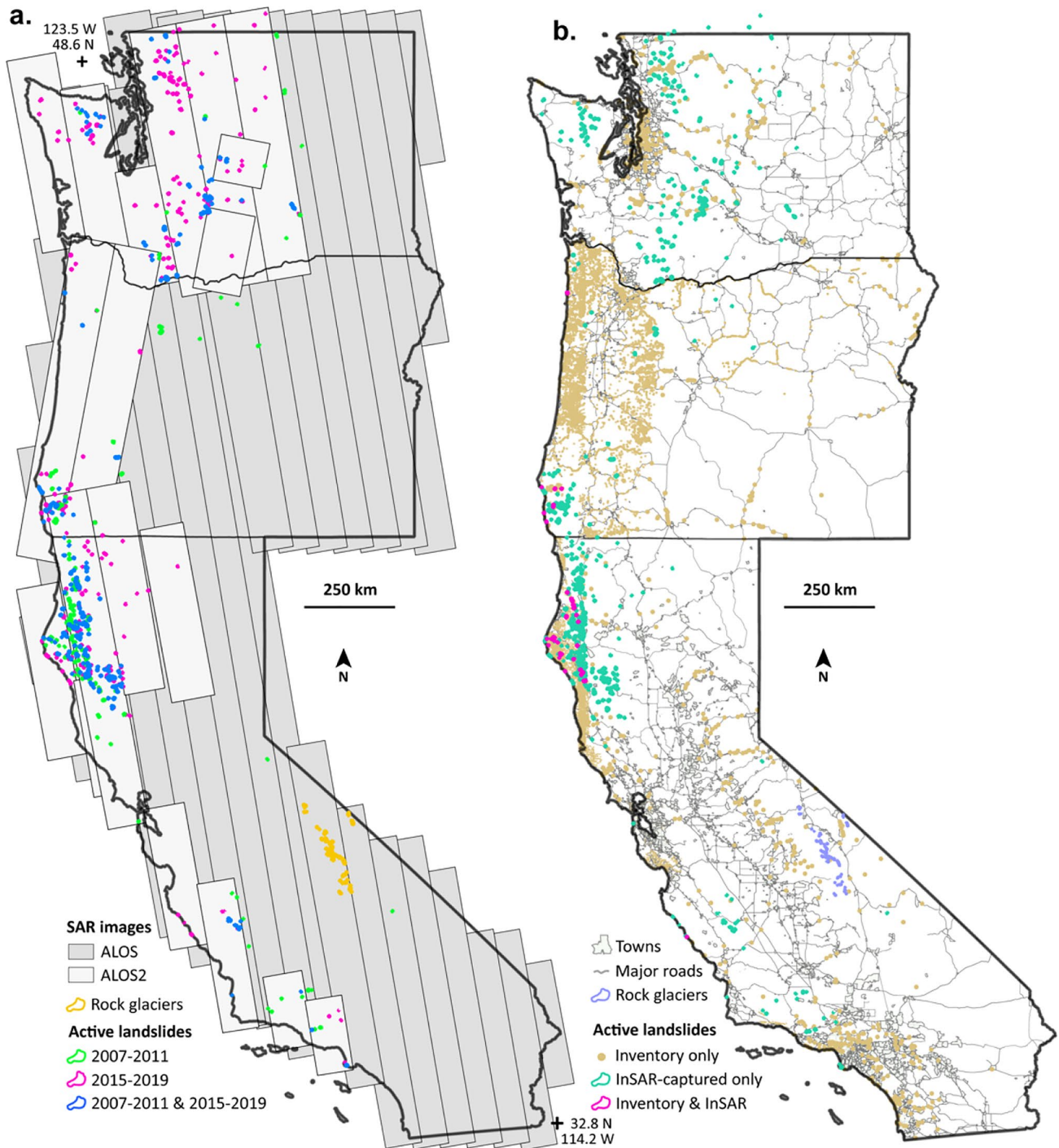


**Fig. 1** SAR imagery coverage and comparison of InSAR-captured landslides and the national landslide inventory. **(a)** Gray-shaded rectangles illustrate spatial extent of the ascending ALOS PALSAR images used (2007–2011), and the white-shaded rectangles represent spatial coverage of the ALOS-2 PALSAR-2 images (2015–2019). The ALOS images spatially cover the entire US West Coast, and the ALOS-2 images are primarily distributed over the western regions

and cover 97.6% of the identified landslides. **(b)** The InSAR-captured landslides denote active landslides detected by ALOS (2007–2011) and/or ALOS-2 (2015–2019) radar images. The landslide inventory (Jones et al. 2019) was compiled from multiple sources and includes landslides recorded between 1932 and 2018, but only as point locations

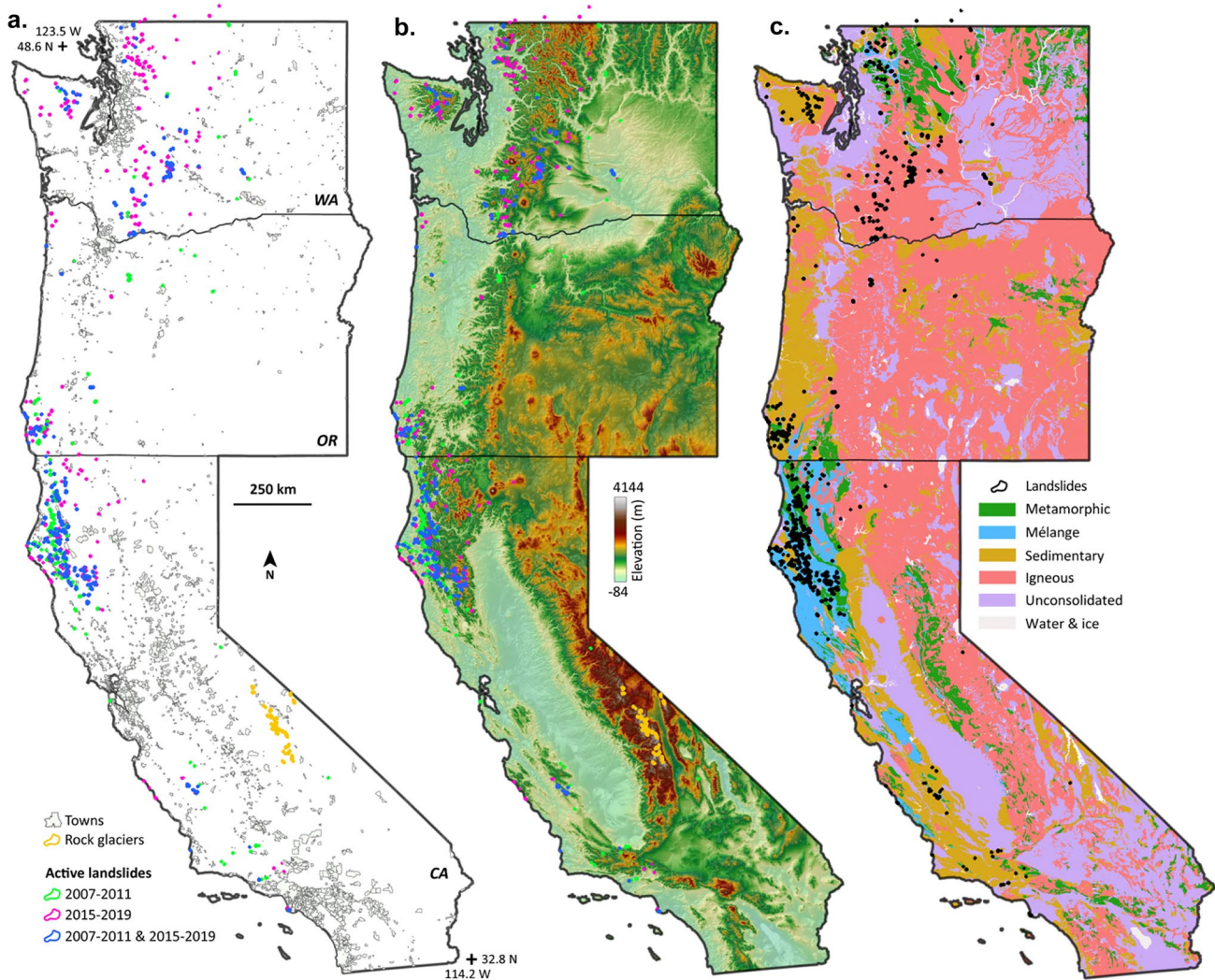


**Fig. 2** Active landslides detected by radar satellites. (a) Spatial distribution of the detected landslides and towns in the US West Coast. The states are annotated as WA, Washington; OR, Oregon; and CA, California. Geographical locations of towns were obtained from US Cen-

sus Bureau (2017 census; USCB 2020). (b) Hillshade map produced from the 10-m DEMs (USGS 2020b). (c) Generalized geological map produced from the SGMC geodatabase (Horton et al. 2017)

the identified 617 landslides (78.4%). We selected only these 16 formations for detailed statistical analyses and categorized them into four distinct types: metamorphic rocks, mélangé, sedimentary rocks, and igneous rocks (including volcanic flows) (Fig. 2c). Note that in the analysis, we utilized adjacent hillslope material to revise the formation for 11 landslides that were supposedly in unconsolidated materials (see section “[Bedrock of the landslides](#)”). Particularly, we investigated the spatial density and spatial size of the landslides with regard to various lithology. Here, spatial density is defined as the ratio of landslide area overlaying a specific bedrock formation by the total area of the bedrock formation.

Our results demonstrate that both spatial density and size of the identified slow-moving landslides were strongly controlled by their lithology. By bedrock type, the greatest spatial density was found in metamorphic rocks (15,300 m<sup>2</sup>/km<sup>2</sup>), followed by mélangé (5400 m<sup>2</sup>/km<sup>2</sup>), sedimentary rocks (3200 m<sup>2</sup>/km<sup>2</sup>), and igneous rocks

(1300 m<sup>2</sup>/km<sup>2</sup>) (Fig. 5). Similar trends were also found in their spatial sizes. The largest mean size was in metamorphic rocks (1.52 km<sup>2</sup>), then mélangé (0.6 km<sup>2</sup>), and similar in sedimentary (0.44 km<sup>2</sup>) and igneous rocks (0.43 km<sup>2</sup>) (Fig. 6). Overall, landslides were largest and most frequent in metamorphic rocks followed by mélangé, and the spatial density and mean size were 3 to 12 times greater in metamorphic rocks than in sedimentary and igneous rocks. The results also indicate that these presently active landslides are presenting hazards from and modifying landscapes of metamorphic and mélangé bedrocks to the greatest extent. Assuming similar area-volume scaling (Larsen et al. 2010) for landslides in each of the bedrock types, the results indicate that slow-moving landslides in mélangé have mobilized 1.4, 8.6, and 10.6 times the sediment of landslides in metamorphic, igneous, and sedimentary rocks, respectively.

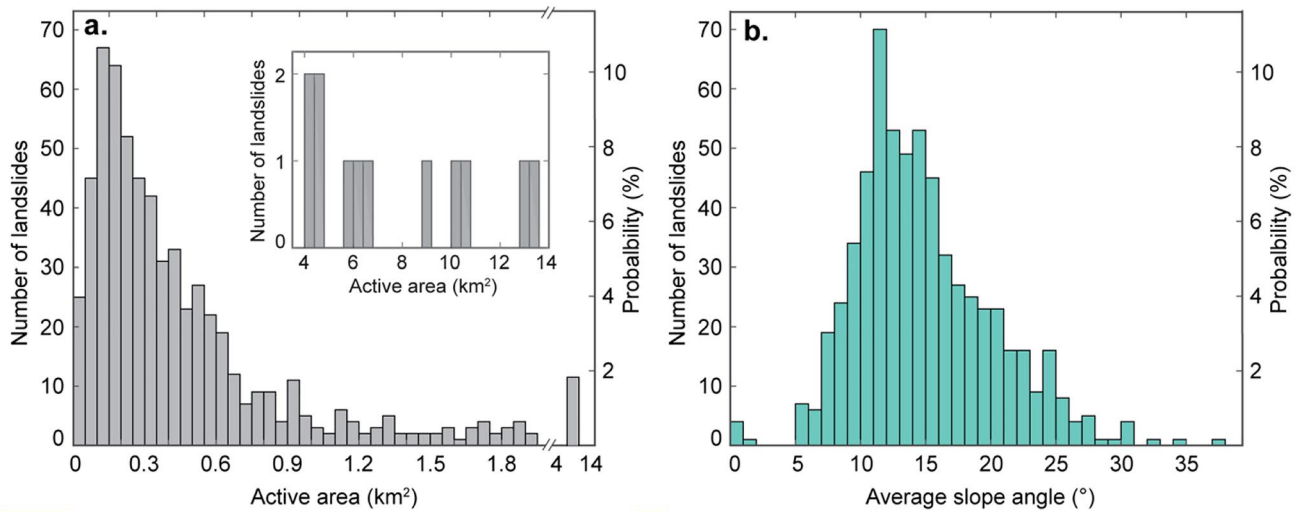


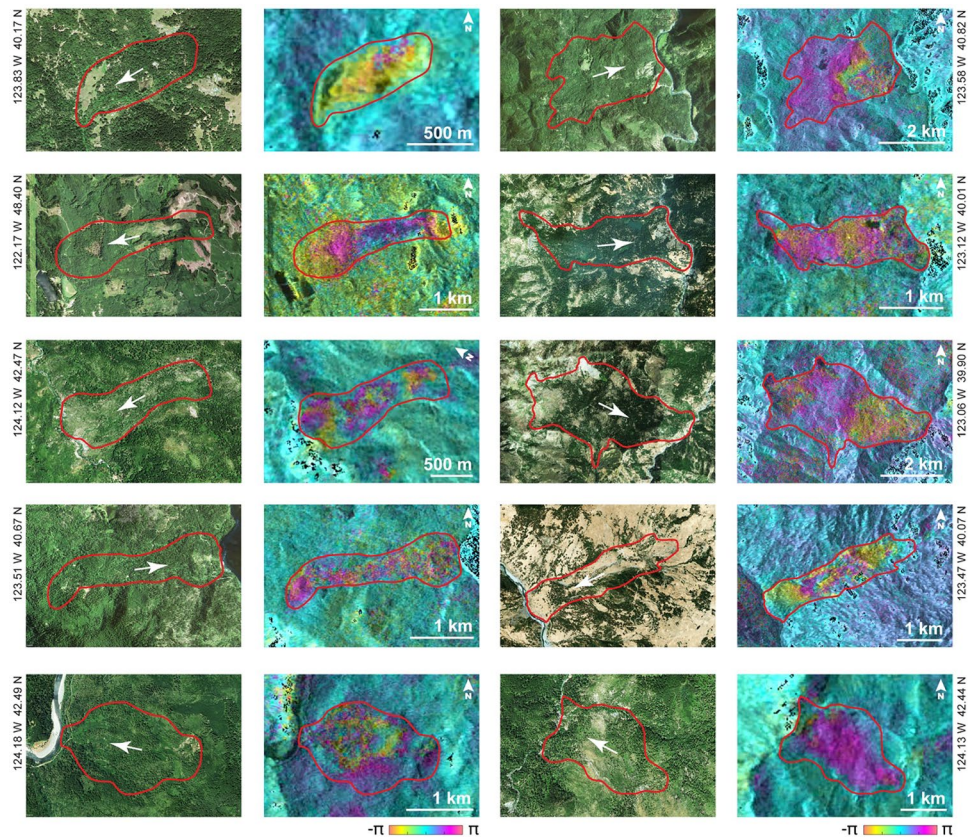
**Fig. 3** Surface geometry of the identified landslides. **(a)** Probability distribution of active areas of the 617 slow-moving landslides. The figure in the upper-right corner is an enlarged illustration of land-

slides larger than 4 km<sup>2</sup>. **(b)** Probability distribution of average slope angles (derived from 10-m DEMs) of the identified landslides

The greater size and density of slow-moving landslides in metamorphic rocks and *mélange* compared to igneous and sedimentary rocks may partly result from generally lower rock mass strength due to pervasive discontinuities in foliated and tectonically sheared metamorphic rocks and *mélange* (Cruden and Varnes 1996), as well as the relatively high abundance of clay minerals in these altered rocks (Lambe and

Whitman 1969; Schmidt and Montgomery 1995). In addition, igneous rocks in which landslides were identified were mostly andesite and basalt flows (Supplementary Material Table S1). Volcanic flows and sedimentary rocks are likely to have spatially extensive discontinuities between beds and flow units, and relatively high anisotropy of material properties because of their layered nature (Jaeger et al. 2007). Such

**Fig. 4** Examples of active landslides discovered by SAR interferograms. This figure illustrates ten exemplary pairs of presently active slow-moving landslides that were generally unidentifiable from submeter-resolution optical images (columns 1 and 3) but were clearly revealed by SAR interferograms (columns 2 and 4). These ten landslides were distributed over Washington, Oregon, and California (geographical coordinates are shown in degrees beside each landslide). Red polygons outline the landslide extents, and white arrows mark the downslope directions. All the optical images were acquired in 2019 and accessed from Google Earth. All the SAR interferograms were produced from ALOS-2 SAR images acquired between May 2018 and August 2019. One fringe (changes from  $-\pi$  to  $\pi$ ) on the SAR interferograms represents a line-of-sight movement of 12.1 cm



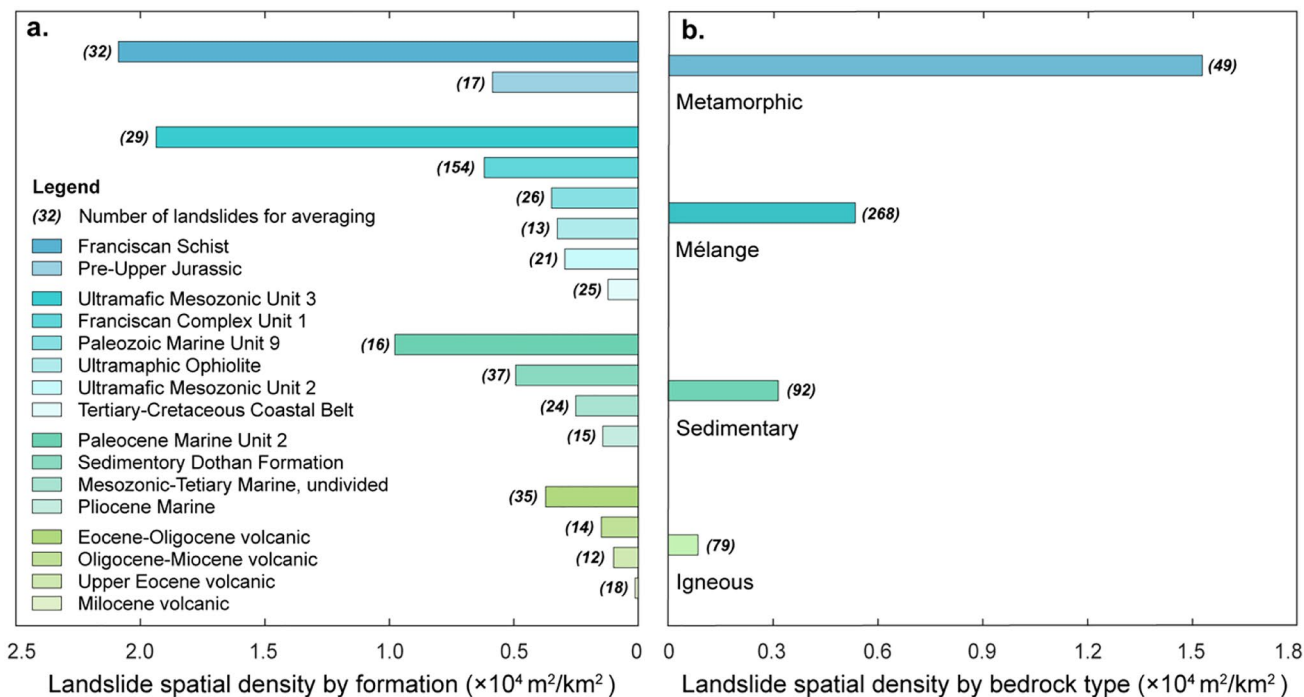


**Fig. 5** Landslide spatial density by bedrock. (a) Average landslide spatial densities by the 16 different formations on which more than ten landslides were identified. For descriptions of the bedrock forma-

tions, refer to Supplementary Material Table S1. (b) Average landslide spatial densities by the four general bedrock types

discontinuities and anisotropy are relatively lacking from most metamorphic and mélangé rock formations (Jaeger et al. 2007). Shallower and therefore smaller landslides are more likely in materials with such

anisotropy (Cruden and Varnes 1996), whereas deeper and therefore larger landslides are more likely in more isotropic materials (Cruden and Varnes 1996), such as mélangé and metamorphic rocks.

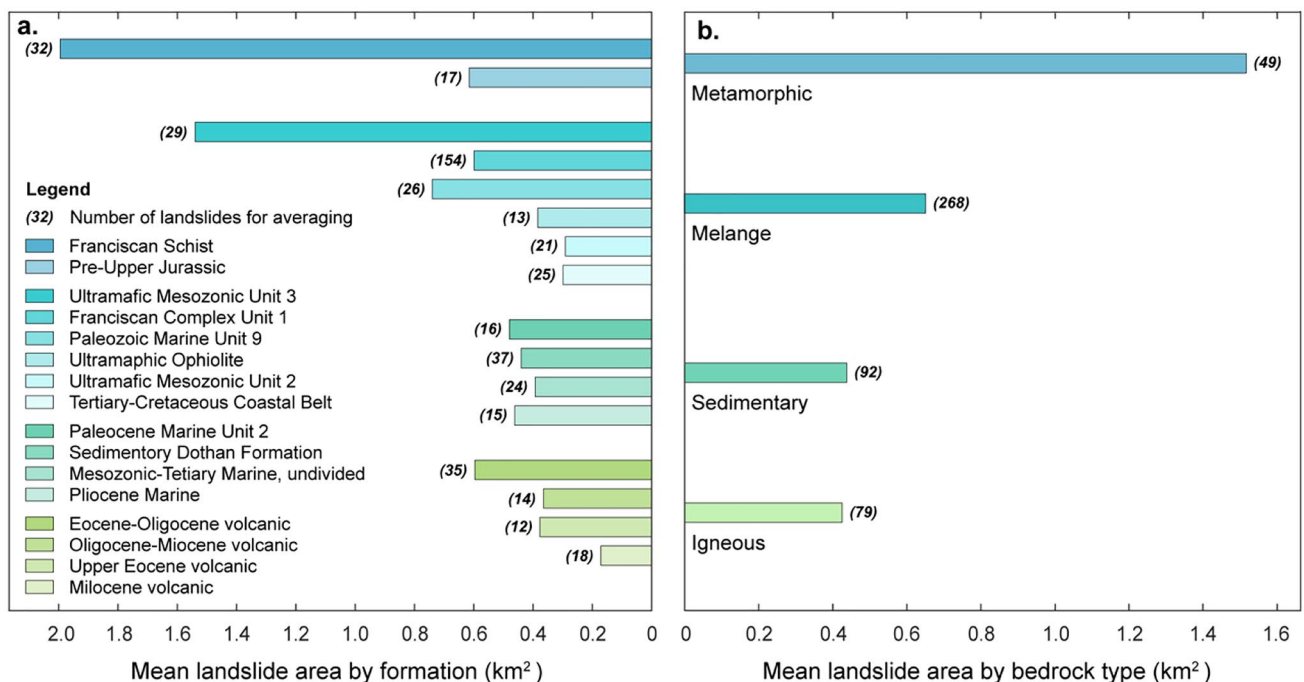


**Fig. 6** Landslide size by bedrock. (a) Average landslide size by the 16 formations. For descriptions of the formations, refer to Supplementary Material Table S1. (b) Average landslide size by the four general bedrock types

## Landsliding contributed by land uplift

We investigated how vertical land motion may relate to the identified slow-moving landslides by incorporating vertical motion data for the study area from radioisotope dating, modeling, and recent GPS observations (Table 1). We expect that land uplift results in and sustains continuous landsliding because uplift creates topographic relief resulting in stream downcutting and hillslope instability (Bennett et al. 2016a; Burbank et al. 1996; Cruden and Varnes 1996; Lambe and Whitman 1969; Roering et al. 2005; Larsen and Montgomery 2012). Slow-moving landslides identifiable from InSAR may be very long lived ( $10^2$ – $10^4$  years) (Bovis and Jones 1992; Keefer and Johnson 1983; Mackey et al. 2009; Varnes and Savage 1996) and usually continue moving during dry periods or reactivate thereafter (Bennett et al. 2016b; Bovis and Jones 1992; Coe 2012; Skempton et al. 1989); thus, their occurrence and persistent long-term creeping motions most likely have been greatly contributed to and/or sustained by geologically recent ( $10^3$ – $10^5$  years) uplift. However, although less sensitive to recent rainfall than small landslides, large landslides are strongly modulated by precipitation on a short time-scale such as seasonal movement (Bennett et al. 2016b; Coe 2012). Here, we only focus on the potential contributions from long-term land uplift, and the short-timescale hydrological contributions are detailed in the “Discussion” section.

Land surface uplift measurements from a total of 79 sites over the study area were converted to gridded data using the inverse distance weighted interpolation in order to compare uplift rates at landslide locations to those at stable regions. We excluded the regions with slope angle less than  $5^\circ$  in the analysis as our observations show that landslides rarely occur in such flat terrain (Fig. 2). Our analyses reveal that the 617 landslides and the 89 rock glaciers were geographically related to geologic uplift. Overall, the rapidly uplifting northwestern Washington, southwestern Oregon, northwestern California, coastal regions of southern California, and the Sierra Nevada of middle-east California all saw a great number of active landslides or rock glaciers, while the subsiding middle-west Oregon, middle-west California, and the southern end of the Sierra Nevada (middle-east California) were barely involved with any identified landslides (Fig. 7). Quantitatively, the uplift rates at the active landslides and rock glaciers average 0.83 mm/year, three times higher than the mean rate of 0.27 mm/year for the whole region (Table 2). The results are also insensitive to the excluded flat regions: thresholding slope angles at  $0^\circ$ ,  $10^\circ$ , and  $16^\circ$  would yield mean uplift rates of 0.79 mm/year over 0.12 mm/year (landslides versus the whole region), 0.83 mm/year over 0.30 mm/year, and 0.82 mm/year over 0.32 mm/year, respectively (Table 2). All of the results provide evidence that the identified slow-moving landslides were preferentially located in areas with accelerated geologically recent uplift. We expect that rapid and/or small landslides similarly collocate with accelerated uplift, but InSAR does not well resolve rapid and/or small landslides.

## Discussion

### Landslide identification using radar interferometry

Despite the high efficiency and effectiveness, landslide mapping using InSAR also faces a few challenges. First, InSAR is relatively less sensitive to landslide motions that are oriented perpendicular to the radar

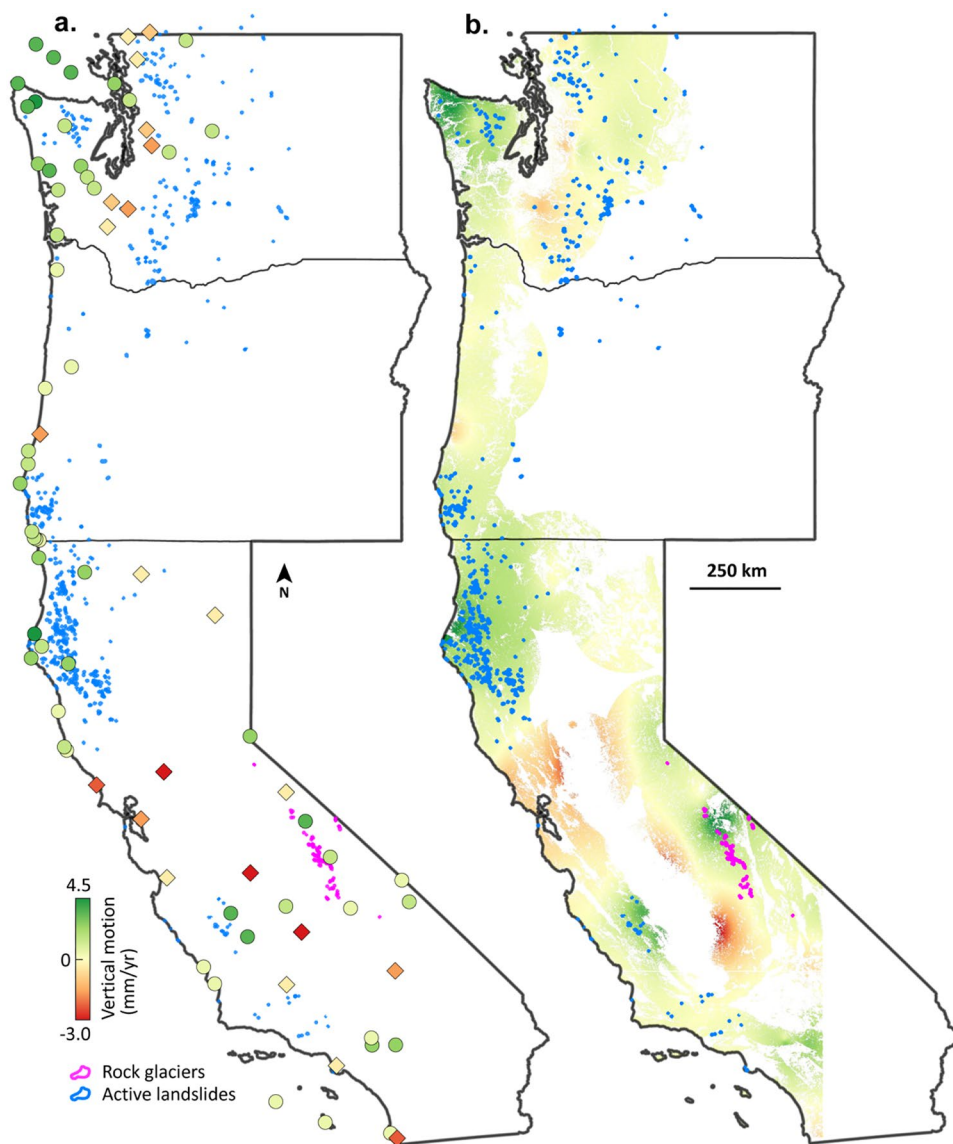
look direction. Mountain ranges near the US West Coast are dominantly north–south orientated and have formed landslides which are mostly visible from the approximately west/east looking radar sensor. We also utilized SAR interferograms spanning as long as 2 years for landslide identification, and such long timespan allows landslides to accumulate a large displacement to be more clearly identifiable on SAR interferograms. Second, coherence loss in particularly densely forested regions may hinder InSAR’s capability to reveal active landslides because of the induced high background noise level. In general, the longer-wavelength L-band imagery we utilized in this study allows better vegetation penetration than the X- and C-band data and therefore was able to produce less noisy SAR interferograms for landslide identification over the relatively densely vegetated US West Coast (e.g., Xu et al. 2021). Note that the short-wavelength X- and C-band SAR images possess better sensitivity to ground deformation than L-band data and hence may perform well in urban environments. Third, small and/or catastrophic landslides are highly challenging to be captured by InSAR. Small landslides occupy only a few pixels on SAR interferograms and may produce deformation signals indistinguishable from localized background noises. Catastrophic landslides such as debris flows often alter landslide surface considerably leading to severe coherence loss and hence cannot be measured by InSAR. However, large catastrophic landslides may be mapped with SAR intensity or coherence images (e.g., Jung and Yun 2020; Plank et al. 2016; Xu et al. 2021). In this study, we focused on large, slow-moving landslides, and therefore the potentially undetected small or catastrophic landslides by InSAR over the eastern mountains of the study region were not specifically considered.

Comparison with the US Geological Survey (USGS) landslide inventory (Fig. 1) shows that our InSAR-based mapping captured much fewer active landslides in northwestern Oregon and the Sierra Nevada in California. One most likely reason is that the USGS inventory comprises many small and/or catastrophic landslides which are challenging to be detected by InSAR. Another potential reason is that some landslides were no longer active during our InSAR observation periods from 2007 to 2011 and from 2015 to 2019. The data gap between 2011 and 2015 results from a lack of free L-band SAR data. Additionally, our InSAR observations only mapped large, active rock glaciers in the study region, and a more complete global rock glacier database can refer to GLIMS and NSIDC 2018. Most rock glaciers are identifiable from optical imagery based on their distinctive geomorphological features.

### Geologic impacts on landslide character and kinematics

We found that bedrock lithology exerts significant control on both the spatial density and size of the slow-moving landslides. Metamorphic rocks and mélangé that have relatively homogeneous composition, discontinuity distribution, and high clay content, while also having relatively low shear strength, are most likely to harbor widespread, deep, and large slow-moving landslides. In contrast, sedimentary and igneous flow rocks that have strength and hydrologic anisotropy and relatively high shear strength tend to produce relatively sparse, shallow, and small slow-moving landslides. In general, bedrock weathering and fracturing also contribute to landslide occurrence by reducing rock mass strength.

**Fig. 7** Vertical land motions near the US West Coast. **(a)** Vertical uplift (green circles) and subsidence (red diamonds) rates of the 79 sites. **(b)** An interpolated map produced from the point-wise measurements. Only hillslopes steeper than 5° and within 100 km distant from the measurement sites are shown in the figure



Our observations also provide evidence that geologic uplift is a crucial contributor to the occurrence and long-term creeping behavior of the slow-moving landslides. Both the identified active rock

glaciers and slow-moving landslides are predominantly distributed over hillslopes with geologically recent ( $10^3$ – $10^5$  years), accelerated uplift, but barely observed in geologically subsiding terrains,

**Table 2** Uplift rates by excluding flat regions. Regions with slope less steep than the slope angle threshold (the first column of the table) were excluded in the corresponding analyses

Slope angle threshold (°)	Regions	Minimum rate (mm/year)	Maximum rate (mm/year)	Mean rate (mm/year)	Standard deviation (mm/year)
0	Landslides	-0.62	2.86	0.79	0.59
	All regions	-3	5	0.12	0.65
5	Landslides	-0.62	2.86	0.83	0.58
	All regions	-2.99	4.72	0.27	0.57
10	Landslides	-0.62	2.86	0.83	0.56
	All regions	-2.96	4.72	0.3	0.56
16	Landslides	-0.62	2.86	0.82	0.53
	All regions	-2.95	4.72	0.32	0.55

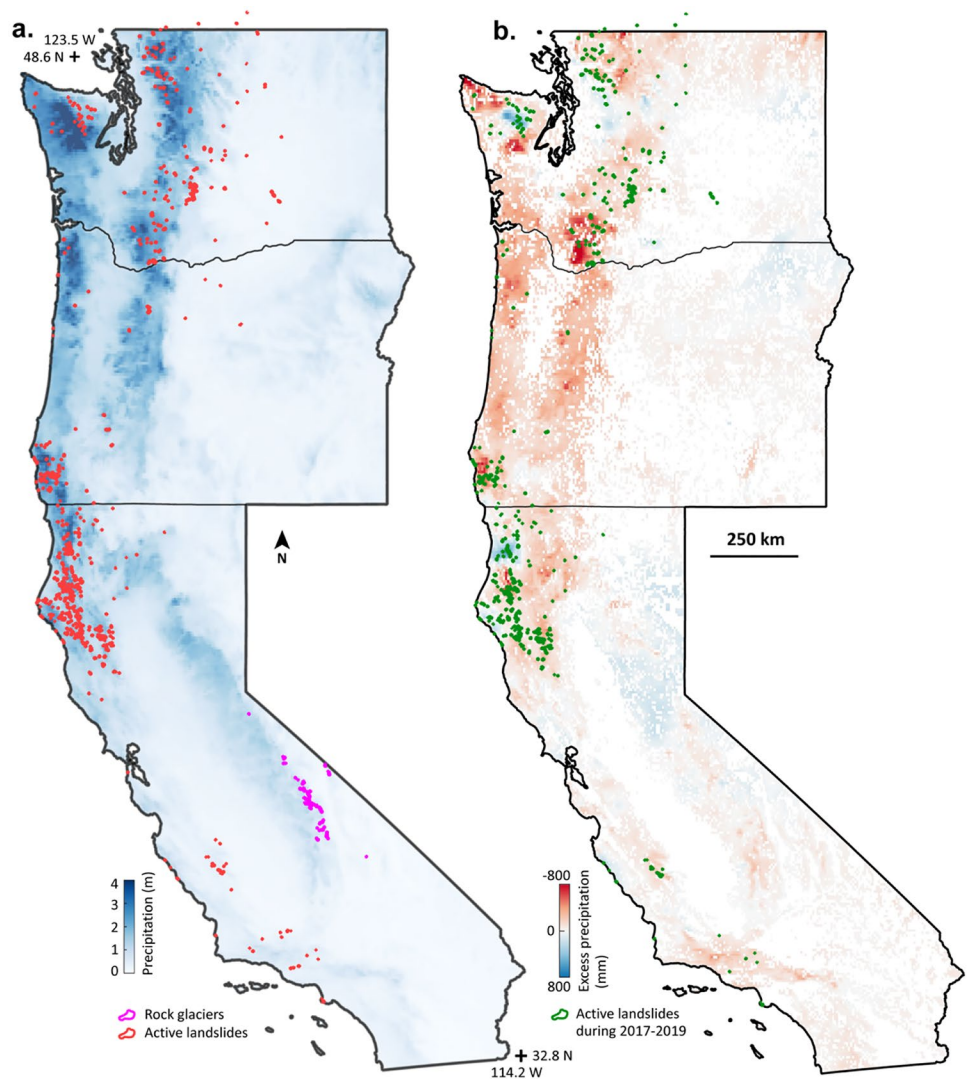
implying a fundamental control from vertical land motion. The contributions from land uplift are a gradually cumulative effect, and such signal could be overwhelmed and clouded by other short-timescale factors (particularly precipitation). Long-term land uplift creates mountains resulting in hillslope instability, and landslide is the process to restabilize a hillslope. Hence, land uplift essentially results in mountain landslides, though precipitation is often seen as the “trigger” for landslide initiation and seasonal acceleration. In addition, uneven land uplift rates may create geological structures as faults and folds, which could also affect landslide occurrence. Rock glaciers often contain ice cores and their current activities are potentially dominated by air temperature change; however, land uplift over a geological timescale may also have contributed to their movement, because land uplift and stream and glacial erosions together created steepened hillslopes where rock glaciers are more likely to move.

### Hydrological impacts on landslide motion

On an annual scale, precipitation is widely recognized as the driver for seasonal acceleration and deceleration of slow-moving landslides (e.g. Bennett et al. 2016b; Handwerger et al. 2019; Squarzoni

et al. 2003; Xu et al. 2019; Xu et al. 2020a, b; Ye et al. 2004). However, precipitation may not be the only reason to initiate a landslide or keep a slow-moving landslide constantly active for hundreds of years (Bonzanigo et al. 2007; Kelsey and Bockheim 1994; Roering et al. 2015). We compared 30-year average precipitation (1981–2010) relative to observed landslide locations (Fig. 8a) and found that the precipitation amount at those locations is highly variable. Overall, 75% of the identified large and slowly moving landslides are located in the mountain ranges that receive relatively rich rainfall ( $\geq 2000$  mm). However, numerous exceptions were found in central Washington and southwestern California, where relatively dry lands (approximately 400-mm annual rainfall) produced about 90 landslides. Moreover, the rainfall-abundant (over 2500 mm) southern Cascade Range and northern Coastal Ranges of Oregon only included 12 landslides, far fewer than the northwestern California where 1800 mm of annual rainfall produced 484 landslides (Fig. 8). In addition, we compared the identified landslides with the average excess precipitation between 2016 and 2019 (Fig. 8b). Here, excess precipitation is defined as the difference between annual precipitation and the 30-year average. The results show that numerous landslides particularly in southern

**Fig. 8** Comparison of landslide distribution and precipitation near the US West Coast. **(a)** 30-year average precipitation from 1981 to 2010 (PRISM Climate Group, 2021). The red polygons depict active landslides captured by ALOS and ALOS-2 images, and the magenta polygons depict active rock glaciers captured by ALOS imagery. **(b)** Excess precipitation (average annual precipitation subtracts the 30-year average) from 2017 to 2019. The green polygons only depict landslides that were active between 2017 and 2019



Washington and southwestern Oregon were captured active during even the historically dry years between 2016 and 2019. Consequently, precipitation alone cannot well explain the spatial distribution of the identified slow-moving landslides.

The precipitation distribution near the US West Coast is not independent from land uplift. In fact, annual precipitation positively correlates with elevation (Daly et al. 2017) because the warm air coming from the Pacific Ocean condenses to form cloud droplets while climbing up the high mountains and produces precipitation. As evidenced in Fig. 8, heavy precipitation dominantly falls on the high mountains of the Coastal Ranges, Cascade Range, and Sierra Nevada. Consequently, land uplift not only leads to landsliding by creating high relief but also contributes to hillslope instability by increasing precipitation over a geological timescale. In addition, the precipitation-elevation relationship indicates that landslide locations' correlation with precipitation may in part result from the correlation with mountain topography, where relatively steep hillslopes reside (see Fig. 2b).

### Implication on landslide and geomorphic studies

Failure events initiated from slow-moving landslides have caused considerable socioeconomic loss globally in recent decades (Froude and Petley 2018; Intrieri et al. 2018; Kilburn and Petley 2003; Schuster and Highland 2001; Xu et al. 2020b), and many damages (especially casualties) could have been avoided if the precursory slow motions were revealed prior to the catastrophes. The routinely acquired (optimal every 6 days; ESA 2020) and globally covered satellite radar images could prove valuable in uncovering such presently active landslides for mitigating future hazards, especially in response to the predicted increasingly frequent landslide activities owing to global climate change and expanding anthropogenic activities (Froude and Petley 2018; Gariano and Guzzetti 2016). In addition, our finding of fundamental controls of slow-moving landslides by bedrock and vertical land motion could offer novel insights into landslide susceptibility forecasting and landform evolution studies. Globally, the geologically recent uplifts in the Himalayan mountains (Asia) (Ader et al. 2012), Alps mountains (Europe) (Sternai 2019), Pacific West Coast (North America) (Muhs et al. 1992), and Andes mountains (South America) (Armijo et al. 2015) are expected to fuel continued landslide hazards and intensify geomorphological change. However, regional tectonic subsidence within these mountain ranges may conversely attenuate local landslide activities.

### Conclusions

We discovered 617 active, large, potentially dangerous landslides over the US West Coast states, 588 of which are missing from existing landslide inventories that source from non-systematically mapped and compiled geologic maps, documentation of precipitation events, and citizen reports (Jones et al. 2019). We found that the high-accuracy InSAR tool could be effective in uncovering their locations, boundaries, and motions.

Our study also suggests that bedrock types exert fundamental control on landslide size and spatial density in general. The relatively weak and homogenous metamorphic rocks and mélange are more susceptible to large, slow-moving landslides than sedimentary and igneous rocks. In addition, regions with rapid land uplift over a geological scale are more likely to experience landslide

activities. Hence, vertical landslide motion rates may be an effective indicator for forecasting landslide susceptibility around the globe.

Precipitation strongly affects the spatial distribution of landslides over the US West Coast. However, over a large spatial scale, a single fixed precipitation threshold may not be applicable to variable regions for forecasting landslide occurrence. Regions with less rainfall may experience more landslide activities partly depending on other factors such as bedrock formation, land uplift, and tectonic activity.

### Acknowledgements

We acknowledge the Japan Aerospace Exploration Agency for acquiring the ALOS PALSAR and ALOS-2 PALSAR-2 images, and we thank the 3D Elevation Program Group of the US Geological Survey (USGS) for producing and making available the 10-m-resolution DEMs. We also thank the authors listed in Table 1 for the uplift data.

### Funding

This study was funded by NASA Interdisciplinary Research (IDS) in Earth Science Program (80NSSC17K0022), NASA Earth Surface and Interior Focus Area (80NSSC19K1317), NASA Science Team (80NSSC19K1491), and the USGS Landslide Hazards Program. Any use of trade, firm, or product names is for descriptive purposes only and does not imply endorsement by the US Government.

### Data and materials availability

The ALOS PALSAR data are freely accessible from the Alaska Satellite Facility (<https://asf.alaska.edu/>), and the ALOS-2 PALSAR-2 data are obtainable from Japan Aerospace Exploration Agency (<https://auig2.jaxa.jp/>). The 10-m-resolution DEMs covering the US West Coast states are freely available from the US Geological Survey (<http://usgs.gov/NationalMap/data/>), and the high-resolution true color images are available from Google Earth. Shapefiles of towns and state boundaries of the US West Coast states are downloadable from the US Census Bureau (<https://www.census.gov/cgi-bin/geo/shapefiles/>). The State Geologic Map Compilation (SGMC) geodatabase of the conterminous United States is available from the US Geological Survey (USGS 2020a). The PRISM precipitation data are freely available from the PRISM Climate Group (<https://prism.oregonstate.edu/>). Shapefiles depicting landslides identified during this study are available from the US Geological Survey ScienceBase repository (Xu et al. 2020a).

### References

- Ader T et al (2012) Convergence rate across the Nepal Himalaya and interseismic coupling on the Main Himalayan Thrust: implications for seismic hazard. *JGR Solid Earth* 117:B04403
- Amos CB et al (2014) Uplift and seismicity driven by groundwater depletion in central California. *Nature* 509:483–486
- Anderson TK (2008) Inferring bedrock uplift in the Klamath Mountains Province from river profile analysis and digital topography. MS Thesis. Texas Tech University: 314p
- Armijo R, Lacassin R, Coudurier-Curveur A, Carrizo D (2015) Coupled tectonic evolution of Andean orogeny and global climate. *Earth-Sci Rev* 143:1–35

- Barth AP, May DJ (1992) Mineralogy and pressure-temperature-time path of Cretaceous granulite gneisses, south-eastern San Gabriel Mountains, southern California. *J Metamorph Geol* 10:529–544
- Bennett GL, Miller SR, Roering JJ, Schmidt DA (2016a) Landslides, threshold slopes, and the survival of relict terrain in the wake of the Mendocino Triple Junction. *Geology* 44:363–366
- Bennett GL, Roering JJ, Mackey BH, Handwerger AL, Schmidt DA, Guillod BP (2016b) Historic drought puts the brakes on earthflows in Northern California. *Geophys Res Lett* 43:5725–5731
- Bonzanigo L, Eberhardt E, Loew S (2007) Long-term investigation of a deep-seated creeping landslide in crystalline rock. Part I. Geological and hydromechanical factors controlling the Campo Vallemaggia landslide. *Can Geotech J* 44:1157–1180
- Bovis MJ, Jones P (1992) Holocene history of earthflow mass movements in south-central British Columbia: the influence of hydroclimatic changes. *Can J Earth Sci* 29:1746–1755
- Burbank DW et al (1996) Bedrock incision, rock uplift and threshold hillslopes in the northwestern Himalayas. *Nature* 379:505–510
- Clarke BA, Burbank DW (2010) Bedrock fracturing, threshold hillslopes, and limits to the magnitude of bedrock landslides. *Earth Planet Sci* 297:577–586
- Coe JA (2012) Regional moisture balance control of landslide motion: implications for landslide forecasting in a changing climate. *Geology* 40:323–326
- Costantini M (1998) A novel phase unwrapping method based on network programming. *IEEE T Geosci Remote S* 36:813–821
- Cruden DM, Varnes DJ (1996) Landslide types and processes, in *Landslides, Investigation and Mitigation: Transportation Research Board Special Report Vol. 247* (eds Turner A, Schuster R) (National Research Council)
- Daly C, Slater ME, Roberti JA, Laseter SH, Swift LW Jr (2017) High-resolution precipitation mapping in a mountainous watershed: ground truth for evaluating uncertainty in a national precipitation dataset. *Int J Climatol* 37:124–137
- ESA (European Space Agency) (2020) Sentinel-1 SAR user guide introduction – revisit and coverage. <https://sentinel.esa.int/web/sentinel/user-guides/sentinel-1-sar/revisit-and-coverage>
- Farr TG et al (2007) The shuttle radar topography mission. *Rev Geophys* 45:RG2004
- Fattahi H, Amelung F (2014) InSAR uncertainty due to orbital errors. *Geophys J Int* 199:549–560
- Ferretti A et al (2007) Submillimeter accuracy of InSAR time series: experimental validation. *IEEE T Geosci Remote* 45:1142–1153
- Froude MJ, Petley D (2018) Global fatal landslide occurrence from 2004 to 2016. *Nat Hazard Earth Sys* 18:2161–2181
- Gariano SL, Guzzetti F (2016) Landslides in a changing climate. *Earth-Sci Rev* 162:227–252
- GLIMS and NSIDC (2018) Global Land Ice Measurements from Space glacier database. <http://www.glims.org/maps/glims>
- Guzzetti F et al (2012) Landslide inventory maps: new tools for an old problem. *Earth-Sci Rev* 112:42–66
- Hammond WC, Blewitt G, Kreemer C (2016) GPS imaging of vertical land motion in California and Nevada: implications for Sierra Nevada uplift. *JGR Solid Earth* 121:7681–7703
- Handwerger AL, Fielding EJ, Huang MH, Bennett GL, Liang C, Schulz WH (2019) Widespread initiation, reactivation, and acceleration of landslides in the northern California Coast Ranges due to extreme rainfall. *JGR Earth Surf* 124:1782–1797
- Hanssen RF (2001) *Radar interferometry: data interpretation and error analysis*. Springer: 308p
- Hellwig JL (2010) The interaction of climate, tectonics, and topography in the Olympic Mountains of Washington State: the influence of erosion on tectonic steady-state and the synthesis of the alpine glacial history. MS Thesis. University of Illinois at Urbana-Champaign: 341p
- Highland L, Bobrowsky PT (2008) *The landslide handbook: a guide to understanding landslides*. US Geol Surv Circular 1325:129p
- Horton JD, San Juan CA, Stoesser DB (2017) *The State Geologic Map Compilation (SGMC) geodatabase of the conterminous United States* (ver. 1.1, August 2017). US Geological Survey Data Series 1052
- House MA (1999) Bedrock uplift of the San Gabriel Mountains: linking long-term rates to modern observations. *SCEC Annual Report*: 4p
- Intrieri E et al (2018) The Maoxian landslide as seen from space: detecting precursors of failure with Sentinel-1 data. *Landslides* 15:123–133
- Jaeger JC, Cook NG, Zimmerman R (2007) *Fundamentals of rock mechanics* (4th ed). John Wiley & Sons
- Jones CH (1987) Is extension in Death Valley accommodated by thinning of the mantle lithosphere beneath the Sierra Nevada, California? *Tectonics* 6:449–473
- Jones ES et al (2019) Summary metadata – Landslide inventories across the United States: U.S. Geological Survey data release. <https://doi.org/10.5066/P9E2A37P>
- Jung J, Yun SH (2020) Evaluation of coherent and incoherent landslide detection methods based on Synthetic Aperture Radar for rapid response: a case study for the 2018 Hokkaido landslides. *Remote Sens* 12(2):265
- Kang Y, Lu Z, Zhao C, Xu Y, Kim JW, Gallegos AJ (2021) InSAR monitoring of creeping landslides in mountainous regions: a case study in Eldorado National Forest, California. *Remote Sens Environ* 258:112400
- Keefer DK, Johnson AM (1983) Earth flows: morphology, mobilization, and movement. *US Geol Surv Prof Paper* 1264:61p
- Kelsey HM, Bockheim JG (1994) Coastal landscape evolution as a function of eustasy and surface uplift rate, Cascadia margin, southern Oregon. *Geol Soc Am Bull* 106:840–854
- Kilburn CR, Petley DN (2003) Forecasting giant, catastrophic slope collapse: lessons from Vajont, Northern Italy. *Geomorphology* 54:21–32
- Kobor JS, Roering JJ (2004) Systematic variation of bedrock channel gradients in the central Oregon Coast Range: implications for rock uplift and shallow landsliding. *Geomorphology* 62:239–256
- Lambe TW, Whitman RV (1969) *Soil mechanics*. Wiley:553p
- Larsen IJ, Montgomery DR (2012) Landslide erosion coupled to tectonics and river incision. *Nat Geosci* 5:468–473
- Larsen IJ, Montgomery DR, Korup O (2010) Landslide erosion controlled by hillslope material. *Nat Geosci* 3:247–251
- Legros F (2002) The mobility of long-runout landslides. *Eng Geol* 63:301–331
- Levy Y (2019) Structural architecture of the Western and Central Transverse Ranges, California, USA. PhD Dissertation. UC San Diego:120p
- Lock J, Kelsey H, Furlong K, Woolace A (2006) Late Neogene and Quaternary landscape evolution of the northern California Coast Ranges: evidence for Mendocino triple junction tectonics. *Geol Soc Am Bull* 118:1232–1246
- Machette MN, Slate JL, Phillips FM (2008) Terrestrial cosmogenic-nuclide dating of alluvial fans in Death Valley. *California US Geol Surv Prof Paper* 1755:45p
- Mackey BH, Roering JJ, McKean JA (2009) Long-term kinematics and sediment flux of an active earthflow, Eel River, California. *Geology* 37:803–806
- Muhs DR, Rockwell TK, Kennedy GL (1992) Late Quaternary uplift rates of marine terraces on the Pacific coast of North America, southern Oregon to Baja California Sur. *Quat Int* 15:121–133
- Nishiguchi T, Tsuchiya S, Imaizumi F (2017) Detection and accuracy of landslide movement by InSAR analysis using PALSAR-2 data. *Landslides* 14:1483–1490
- Pazzaglia FJ, Brandon MT (2001) A fluvial record of long-term steady-state uplift and erosion across the Cascadia forearc high, western Washington State. *Am J Sci* 301:385–431
- Penserini BD, Roering JJ, Streig A (2017) A morphologic proxy for debris flow erosion with application to the earthquake deformation cycle, Cascadia Subduction Zone, USA. *Geomorphology* 282:150–161
- Plank S, Twele A, Martinis S (2016) Landslide mapping in vegetated areas using change detection based on optical and polarimetric SAR data. *Remote Sens* 8(4):307
- PRISM Climate Group (2021), PRISM climate data. <https://prism.oregonstate.edu>
- Reiners PW et al (2002) Late Miocene exhumation and uplift of the Washington Cascade Range. *Geology* 30:767–770
- Rodriguez E, Martin JM (1992) Theory and design of interferometric synthetic aperture radars. *IEE Proc F (radar and Signal Processing)* 139:147–159

- Roering JJ et al (2015) Beyond the angle of repose: a review and synthesis of landslide processes in response to rapid uplift, Eel River, Northern California. *Geomorphology* 236:109–131
- Roering JJ, Kirchner JW, Dietrich WE (2005) Characterizing structural and lithologic controls on deep-seated landsliding: implications for topographic relief and landscape evolution in the Oregon Coast Range, USA. *Geol Soc Am Bull* 117:654–668
- Roering JJ, Stimely LL, Mackey BH, Schmidt DA (2009) Using DInSAR, airborne LiDAR, and archival air photos to quantify landsliding and sediment transport. *Geophys Res Lett* 36:L19402
- Schmidt KM, Montgomery DR (1995) Limits to relief. *Science* 270:617–620
- Schulz WH, Wang G (2014) Residual shear strength variability as a primary control on movement of landslides reactivated by earthquake-induced ground motion: implications for coastal Oregon, USA. *JGR Earth Surf* 119:1617–1635
- Schuster RL, Highland L (2001) Socioeconomic and environmental impacts of landslides in the western hemisphere. *US Geol Surv Open-File Report 2001–276:48p*
- Schweickert RA (2009) Beheaded west-flowing drainages in the Lake Tahoe region, northern Sierra Nevada: implications for timing and rates of normal faulting, landscape evolution and mechanism of Sierran uplift. *Int Geol Rev* 51:994–1033
- Simoni A, Ponza A, Picotti V, Berti M, Dinelli E (2013) Earthflow sediment production and Holocene sediment record in a large Apennine catchment. *Geomorphology* 188:42–53
- Skempton AW, Leadbeater AD, Chandler RJ (1989) The Mam Tor landslide, North Derbyshire. *Philos Trans Royal Soc A* 329:503–547
- Spiker EC, Gori PL (2003) National landslide hazards mitigation strategy—a framework for loss reduction. *US Geol Surv Circular* 1244:64p
- Spotila JA, Farley KA, Sieh K (1998) Uplift and erosion of the San Bernardino Mountains associated with transpression along the San Andreas fault, California, as constrained by radiogenic helium thermochronometry. *Tectonics* 17:360–378
- Squarzoni C, Delacourt C, Allemand P (2003) Nine years of spatial and temporal evolution of the La Valette landslide observed by SAR interferometry. *Eng Geol* 68:53–66
- Sternaï P (2019) Present-day uplift of the European Alps: evaluating mechanisms and models of their relative contributions. *Earth-Sci Rev* 190:589–604
- USCB (U.S. Census Bureau) (2020) Topologically Integrated Geographic Encoding and Referencing (TIGER)/Line Shapefiles, <https://www.census.gov/cgi-bin/geo/shapefiles/>
- USCB (U.S. Census Bureau) (2019). Annual estimates of the resident population for the United States, Regions, States, and Puerto Rico: April 1, 2010 to July 1, 2019. Retrieved from <https://www.census.gov/data/tables/time-series/demo/popest/2010s-state-total.html>
- USGS (U.S. Geological Survey) (2020a) U.S. Geological Survey Mineral Resources bedrock geologic units online database, <https://mrddata.usgs.gov/catalog/science.php?thcode=2&term=84>
- USGS (U.S. Geological Survey) (2020b) National Elevation Datasets –1/3 arc-second DEM, <http://usgs.gov/NationalMap/data>
- Unruh JR (1991) The uplift of the Sierra Nevada and implications for late Cenozoic epeirogeny in the western Cordillera. *Geol Soc Am Bull* 103:1395–1404
- Varnes DJ, Savage WZ (1996) The Slumgullion earth flow: a large-scale natural laboratory. *US Geol Surv Bull* 2130:104p
- Werner C, Wegmüller U, Strozzi T, Wiesmann A (2000) Gamma SAR and interferometric processing software. Proceedings of the ERS-Envisat Symposium, Gothenburg, Sweden 1620:9p
- Xu Y, George DL, Kim J, Lu Z, Riley M, Griffin T, de la Fuente J (2021) Landslide monitoring and runout hazard assessment by integrating multi-source remote sensing and numerical models: an application to the Gold Basin landslide complex, northern Washington. *Landslides* 18:1131–1141
- Xu Y, Kim J, George DL, Lu Z (2019) Characterizing seasonally rainfall-driven movement of a translational landslide using SAR imagery and SMAP soil moisture. *Remote Sens* 11:2347
- Xu Y, Lu Z, Kim J, Schulz WH (2020a) Slow-moving landslides near the U.S. West Coast mapped from ALOS and ALOS-2 InSAR, 2007–2019. U.S. Geological Survey data release. <https://www.sciencebase.gov/catalog/item/5f7c952382ce1d74e7db53c3>
- Xu Y, Lu Z, Schulz WH, Kim J (2020b) Twelve-year dynamics and rainfall thresholds for alternating creep and rapid movement of the Hooskanaden landslide from integrating InSAR, pixel offset tracking, and borehole and hydrological measurements. *JGR Earth Surf* 125:e2020JF005640
- Ye X, Kaufmann H, Guo XF (2004) Landslide monitoring in the Three Gorges area using D-InSAR and corner reflectors. *Photogramm Eng Rem S* 70:1167–1172
- Yousefi M, Milne G, Li S, Wang K, Bartholet A (2020) Constraining interseismic deformation of the Cascadia subduction zone: new insights from estimates of vertical land motion over different timescales. *JGR Solid Earth* 125:e2019JB018248

Supplementary information The online version contains supplementary material available at <https://doi.org/10.1007/s10346-021-01732-3>.

**Yuankun Xu** (✉) · **Zhong Lu** · **Jinwoo Kim**

Roy M. Huffington Department of Earth Sciences, Southern Methodist University, Dallas, TX 75205, USA  
Email: [yuankunx@smu.edu](mailto:yuankunx@smu.edu)

**William H. Schulz** · **Kelli Baxstrom**

U.S. Geological Survey, Golden, CO 80401, USA